

PAPER

Surface discharge plasma actuator driven by a pulsed 13.56 MHz–5 kHz voltage waveform

To cite this article: J Dedrick *et al* 2013 *J. Phys. D: Appl. Phys.* **46** 405201

View the [article online](#) for updates and enhancements.

Related content

- [Fast Track Communication](#)
J Dedrick, R W Boswell and C Charles
- [Plasma propagation of a 13.56 MHz asymmetric surface barrier discharge in atmospheric pressure air](#)
J Dedrick, R W Boswell, P Audier *et al.*
- [Control of diffuse and filamentary modes in an RF asymmetric surface barrier discharge in atmospheric-pressure argon](#)
J Dedrick, R W Boswell, H Rabat *et al.*

Recent citations

- [Aerodynamic actuation characteristics of radio-frequency discharge plasma and control of supersonic flow](#)
Zhen Yang *et al*
- [Electrical Characteristics in Surface Dielectric Barrier Discharge Driven by Microsecond Pulses](#)
Cheng Zhang *et al*
- [Diagnostics for characterisation of plasma actuators](#)
Marios Kotsonis



IOP | ebooks™

Bringing together innovative digital publishing with leading authors from the global scientific community.

Start exploring the collection—download the first chapter of every title for free.

Surface discharge plasma actuator driven by a pulsed 13.56 MHz–5 kHz voltage waveform

J Dedrick¹, S Im², M A Cappelli², R W Boswell¹ and C Charles¹

¹ Space Plasma, Power and Propulsion Laboratory, Research School of Physics and Engineering, The Australian National University, ACT 0200, Australia

² Mechanical Engineering Department, Stanford University, Stanford, California 94305-3032, USA

Received 4 June 2013, in final form 25 July 2013

Published 17 September 2013

Online at stacks.iop.org/JPhysD/46/405201

Abstract

The effect of incorporating pulses of radio-frequency (rf: 13.56 MHz) voltage into the driving waveform of a surface discharge plasma actuator is investigated. Rf voltage is applied to the actuator to increase the production of ions and thereby increase the thrust that is generated by the discharge. This waveform is coupled to the powered electrode in 5 μ s pulses and combined with a relatively low-frequency (LF) 5 kHz sinusoid to form a pulsed 13.56 MHz–5 kHz (rf-LF) driving voltage. Measurements of the applied voltage, rf and LF currents, effective power, and velocity field of the surrounding air are undertaken at atmospheric pressure. The thrust that is generated using the rf-LF waveform is estimated from the velocity fields using a momentum balance and is found to increase for increasing rf voltage when the LF voltage remains constant. Maximum thrust is achieved when the rf pulses are positioned at the LF voltage minima and this suggests the importance of negative ions. The efficacy of rf-LF actuation is investigated by comparing the thrust that is generated per unit increase in peak voltage with that obtained using an LF-driven discharge.

(Some figures may appear in colour only in the online journal)

1. Introduction

Surface dielectric barrier discharges (SDBDs) offer a means to actively control, or actuate, aerodynamic boundary layers with no moving parts and relatively low power consumption [1, 2]. When driven by a low-frequency (LF: Hz–kHz) voltage waveform, they have been demonstrated to be effective in modifying the properties of low-speed flows [3–5].

In LF SDBD actuators, as distinct from those that are driven by nanosecond pulses [6–9], flow control is thought to be achieved through an ion–neutral momentum exchange in unipolar (non-neutral) regions of the discharge [10–12]. This results in a reaction force and thrust that can modify flow properties.

Despite promising results in supersonic flows [13], the optimum performance of LF SDBDs is typically observed under low-speed conditions ($Re < 10^5$ [1]). To increase the authority of actuation and widen the scope for their application, extensive research has been undertaken to increase the thrust that is generated by these discharges. This includes efforts

to understand the physical mechanisms that can influence the ion–neutral momentum exchange and force production [14–21], the effect of varying the shape of the powered electrode [22, 23], properties of the dielectric barrier [24, 25], actuator dimensions [26] and the refinement of the applied-voltage waveform [27–30]. LF SDBDs that incorporate three electrodes have also been investigated [31–33].

Since the mechanism for actuation using LF SDBDs is understood to be a momentum exchange between ions and neutrals, the plasma density is an important factor in determining the authority of flow control. For increased thrust, the production of a larger ion density could be of significant benefit so long as the facility for the ion–neutral momentum exchange is preserved. Radio-frequency (rf: 13.56 MHz) voltage sources, for which the amplitude of electron oscillation between the electrodes is small compared to LF waveforms, can facilitate more efficient ionization and a lower breakdown voltage [34]. They can hence be useful in the generation of relatively high-density discharges at atmospheric pressure [35]. It is therefore of interest to investigate whether the

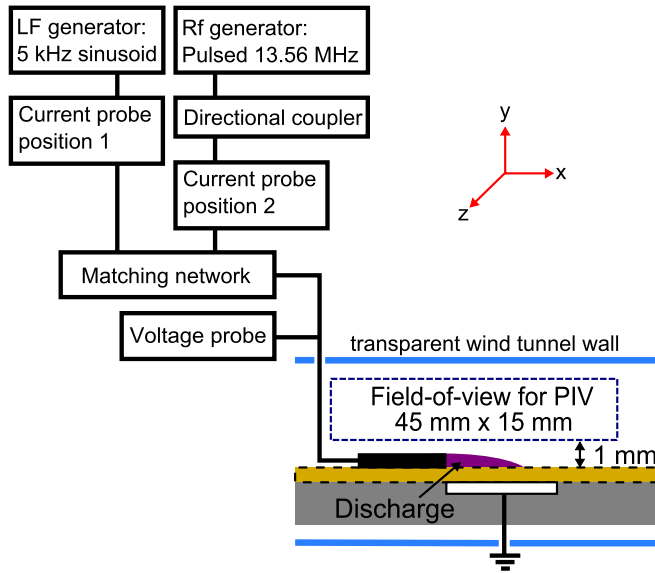


Figure 1. Schematic of the actuator showing a cartoon of the discharge, rf 13.56 MHz and LF 5 kHz generators, positions of the current and voltage probes and the field-of-view for particle image velocimetry (PIV). The length of the actuator is measured along the z-axis. The powered and grounded electrodes are shown in black and white, respectively, and the dielectric layer over which the discharge propagates is enclosed by a dashed line.

application of an rf voltage could be useful in increasing the ion density and thrust that is generated by LF SDBD plasma actuators.

In this study, rf voltage at 13.56 MHz is applied to an SDBD actuator in atmospheric-pressure air. To ensure that there is sufficient time within the period of the applied-voltage waveform for unipolar regions to develop and for ions to be accelerated, drift and exchange their momentum with neutrals, the rf voltage is applied in $5 \mu\text{s}$ pulses and combined with an LF 5 kHz sinusoidal voltage. This enables the position of the rf pulses within the period of the LF voltage waveform, together with the amplitudes of both the rf and LF voltages, to be independently varied and their influence examined with respect to the generation of thrust.

2. Experiment details

2.1. Actuator design

The actuator is comprised of two planar electrodes that are separated by a dielectric barrier as shown in figure 1. The electrodes are $35 \mu\text{m}$ thick copper tape and the dielectric is $80 \mu\text{m}$ thick Kapton tape. The electrode that is exposed to the ambient atmosphere and to which power is coupled is 10 mm wide. The buried electrode, which is electrically grounded, is 19 mm wide. Upon activation, ionization occurs only in the region between the exposed, powered electrode and the dielectric surface. The length of the actuator is 20 cm.

To enable control over the ambient flow field and effective optical access, the actuator is configured inside a $30 \times 30 \text{ cm}^2$ low-speed wind tunnel with transparent walls. To ensure quiescent flow conditions, electrical connections to

the actuator are made via feedthroughs and the wind tunnel fan is not used during data collection.

2.2. Electrical probes

The applied voltage is measured using a high-voltage probe (direct current-75 MHz) and this is installed between the matching network and the powered electrode as shown in figure 1. For measurements of the LF and rf currents, a Rogowski current probe (2 Hz–35 MHz) is fitted in either of two positions: (1) Between the LF generator and matching network or (2) between the rf generator (and directional coupler) and matching network.

The current probe is fitted in two different positions due to the presence of the matching network that is installed between both generators and the actuator as shown in figure 1. This is an LC resonant circuit that is designed to facilitate power coupling between each generator and the actuator and to shield the generators from themselves. It incorporates variable capacitors that have a voltage rating of 5.0 kV and hence this is the upper limited placed upon the total peak voltage that can be applied at the powered electrode.

The current and voltage probes are calibrated into a 50Ω load with a standing-wave-ratio meter. To determine the effective rf power that is coupled to the discharge, a 30 dB directional coupler is installed between the rf generator and the matching network.

2.3. Dual-frequency voltage waveform

A sinusoidal LF voltage, which oscillates at a frequency of 5 kHz (200 μs period), is applied at the powered electrode. The amplitude of the LF voltage is chosen such that rf pulses may be added to form a combined rf-LF waveform with a peak voltage below the 5.0 kV limit as required by the matching network. The voltage and current waveforms that are measured when the current probe is fitted in position (1) are shown in figure 2 for an LF voltage of 3.6 kV. The current waveform exhibits rapid spikes around the positive-going and negative-going zero-crossings of the voltage and these are of larger amplitude when the voltage is rising, e.g. for $100 < t < 200 \mu\text{s}$. These properties are consistent with those previously reported for LF SDBDs in atmospheric-pressure air [22, 36, 37].

Rf power at 13.56 MHz (period 74 ns) is also coupled to the powered electrode in $5 \mu\text{s}$ pulses at a pulse frequency of 5 kHz (period 200 μs). The corresponding voltage and current waveforms are shown in figure 3 for an rf voltage of 1.0 kV. Here, the current probe is fitted in position (2). The rf voltage is observed to rise continuously during the pulse for $5 \mu\text{s} \geq t \leq 10 \mu\text{s}$ and the rf current exhibits peaks at the initiation and completion of the pulse ($t = 5 \mu\text{s}$ and $t = 10 \mu\text{s}$, respectively). These are present whether the discharge is active or not and are thought to be a property of the rf generator that is due to modifications made to enable rapid rise-time pulsing.

The rf and LF waveforms are combined prior to their application at the powered electrode using the matching network. For all experiments, the duration of the rf pulses is $5 \mu\text{s}$ (as shown in figure 3) and the pulse frequency is 5 kHz. Since the oscillation frequency of the LF voltage is identical

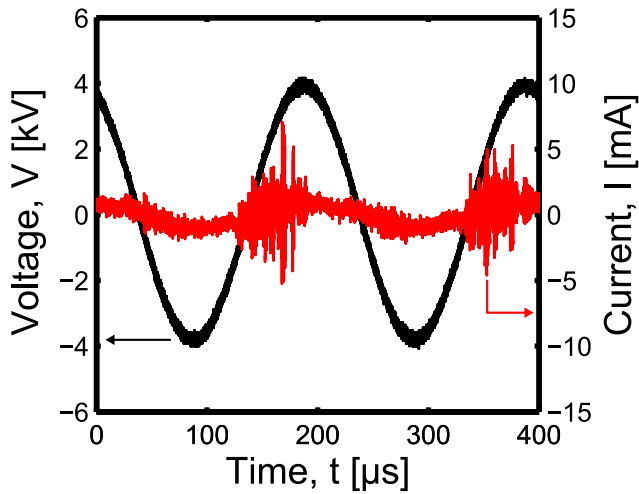


Figure 2. Variation in the applied voltage and current when a 3.6 kV, 5 kHz sinusoidal LF voltage is applied at the powered electrode and the current probe is fitted in position (1) as shown in figure 1.

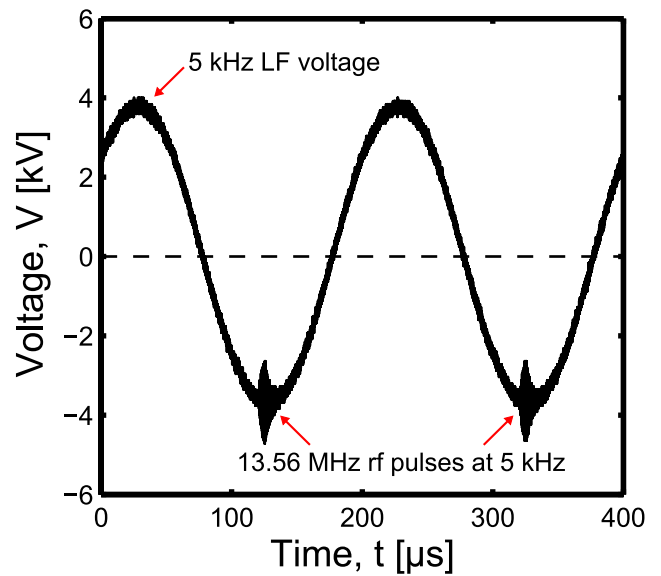


Figure 4. Variation in the rf-LF driving voltage when 5 kHz pulses of rf 13.56 MHz voltage are combined with a 5 kHz LF sinusoid. The LF and rf voltages have an amplitude of 3.6 kV and 1.0 kV, respectively and the rf pulses are positioned at the LF voltage minima.

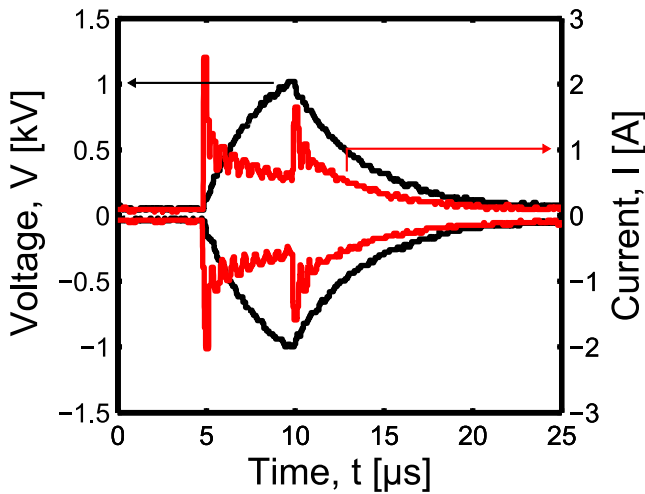


Figure 3. Variation in the rf voltage and current when 1.0 kV, 13.56 MHz rf pulses are applied to the discharge at a frequency of 5 kHz and the current probe is fitted in position (2) as shown in figure 1. The measurements are shown as envelopes to aid visualization.

to the rf pulse frequency, i.e. 5 kHz, the rf-LF driving voltage comprises one rf pulse per LF period as shown in figure 4.

2.4. Measurement of the velocity field

The velocity of the air in the vicinity of the actuator is tracked using particle image velocimetry (PIV). Aluminum oxide (Al_2O_3) particles are introduced into the field-of-view (see figure 1) and are sufficiently small (diameter < 1 mm) that they can accurately follow the velocity of the ambient air [38]. The particles are seeded into the field-of-view from the wind tunnel entrance and are removed from the test section between tests (using the wind tunnel fan) to prevent their accumulation on the actuator model.

The field-of-view for PIV is oriented in the x - y plane ($z = 10$ cm) and its bottom edge is located approximately 1 mm above the plane of the dielectric layer. An Nd:YAG laser

sheet (New wave Gemini PIV, 532 nm, 3 Hz, approximately 1 mm thick) is formed using spherical and cylindrical lenses (not shown in figure 1) and oriented in the same plane as the field-of-view. The light scattered off the tracer particles is detected from the perpendicular direction using a non-intensified charge-coupled-device camera (LaVision, Imager Intense: 1024×1280 pixels) that is fitted with a 50 mm lens and a 532 nm band-pass filter (FWHM 10 nm).

To obtain an instantaneous velocity field, i.e. a two-dimensional distribution of the velocity of the tracer particles within the field-of-view, two single-shot images of the scattered light are acquired with a delay of $700 \mu\text{s}$. The mean velocity field is calculated by averaging over an ensemble of 300 image pairs. All image processing is undertaken using DaVis 7 software. Cross-correlation is completed in two passes (two iterations per pass) with interrogation window sizes of 64×64 pixels and 32×32 pixels and an overlap of 50% in each case. The spatial resolution is 0.75 vectors/mm and the uncertainty of the velocity measurements is conservatively estimated to be 1.15%.

2.5. Estimation of the thrust

To study the performance of the actuator, the thrust that is generated in the direction parallel to the surface of the dielectric barrier layer, i.e. in the x -direction, is estimated from the PIV measurements. This can be achieved by applying a momentum balance to a control volume that encloses the actuation region and assuming that the flow is two-dimensional, steady-state, incompressible and of constant viscosity [38–40]. The control volume that is used in this study is shown in figure 5.

Due to the no-slip condition at the dielectric surface, the momentum flux passing through the bottom side of the control volume a–d is assumed to be zero. Since the flow velocity is

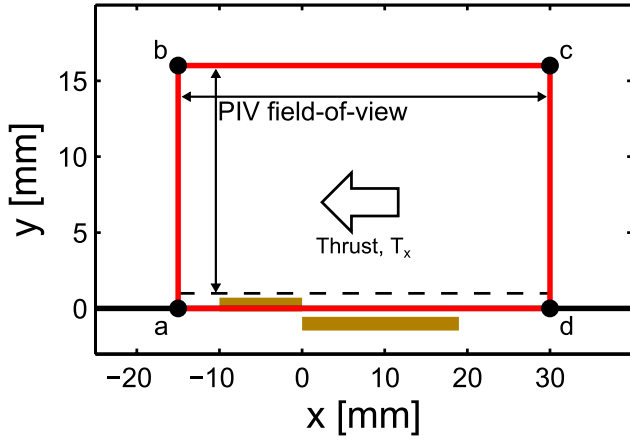


Figure 5. Illustration of the control volume that is used for the estimation of thrust. The line $y = 0$ mm corresponds to the surface of the dielectric layer and the powered and grounded electrodes are shown by the solid lines for $-10 \geq x \leq 0$ mm and $0 \geq x \leq 19$ mm, respectively (thickness not to scale). The control volume is bounded by corners a, b, c and d as shown by the closed circles and the bottom edge of the PIV field-of-view at $y = 1$ mm is shown by the dashed line.

expected from previous studies to be in the positive x -direction [1, 2], i.e. in the opposite direction to the thrust T_x , the left and top sides of the control volume (a–b and b–c, respectively) are designated as boundaries through which momentum flux enters the control volume and the right side (c–d) is the boundary through which momentum flux exits. Using these definitions and assumptions, a momentum balance on the control volume can be written as [39]

$$\frac{T_x}{L_z} = \rho \int_a^b u_x^2 dy + \rho \int_b^c u_x u_y dx - \rho \int_d^c u_x^2 dy + \rho \int_a^b p dy - \rho \int_d^c p dy, \quad (1)$$

where T_x is the x -component of the thrust, which incorporates the body forces due to the discharge and the friction between the moving air and the dielectric surface [40], L_z is the length of the actuator, ρ is the density of atmospheric-pressure air at 25 °C (1.184 kg m^{-3}), p is the static pressure and u_x and u_y are the velocity components in the x and y directions, respectively.

To simplify equation (1), the change in static pressure along the left and right boundaries of the control volume (a–b and c–d, respectively) is not included in the analysis. This is considered to be reasonable because these boundaries are located 15 mm and 30 mm, respectively, from the edge of the powered electrode and hence any change in the static pressure due to the discharge may be relatively small [39, 41]. With this simplification, equation (1) becomes

$$\frac{T_x}{L_z} \approx \rho \int_a^b u_x^2 dy + \rho \int_b^c u_x u_y dx - \rho \int_d^c u_x^2 dy. \quad (2)$$

Since no information concerning the velocity field is acquired for $0 \geq y < 1$ mm, it is expected that the estimates of T_x are conservative. However, previous measurements using PIV and Pitot probe diagnostics suggest that in this region u_x decreases sharply for decreasing values of y due to the presence of the boundary layer [27, 38, 41]. Therefore, its contribution to the total thrust may be relatively small.

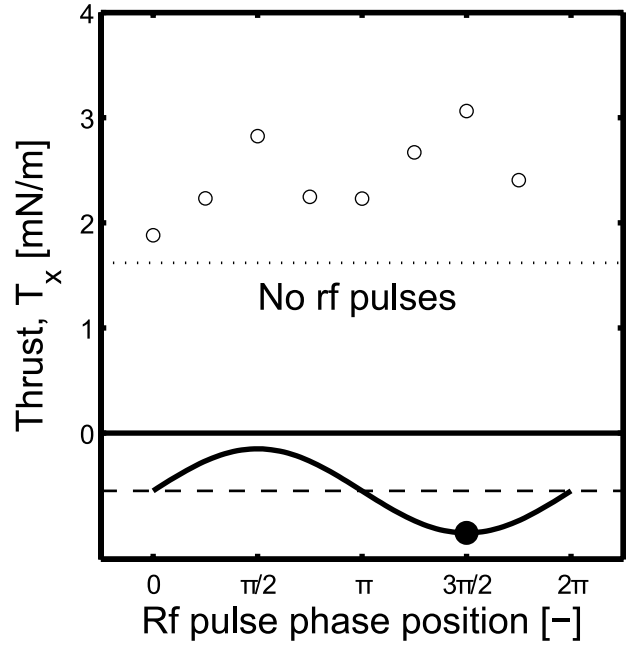


Figure 6. Variation in the thrust T_x measured when rf pulses are applied at different positions within the LF voltage period for an rf-LF driving waveform that comprises a 3.6 kV LF sinusoid combined with 1.0 kV rf pulses. The relative amplitude of the LF voltage at which the rf pulses are positioned is illustrated by the solid curved line. The thrust that is measured when only the LF waveform is applied to the actuator is shown by the dotted line. The pulse position for which the velocity fields are plotted later in figure 7 is $\frac{3\pi}{2}$ as marked by the closed circle.

3. Results

3.1. Position of the rf pulses within the LF period

The position of the rf pulses within the period of the LF voltage, i.e. whether they are applied at the voltage maxima, minima, zero-crossings etc., may be an important factor in determining the amount of thrust that can be generated by the rf-LF actuator. For example, it may be useful to apply the pulses at the LF maxima or minima such that the ions generated by the rf voltage undergo maximum acceleration at the conclusion of each pulse.

To investigate the dependence of the rf pulse position on the generation of thrust, equation (2) is used to estimate the thrust at 8 equally spaced pulse positions within the LF period as shown in figure 6. These are $0, \frac{\pi}{4}, \frac{\pi}{2}, \frac{3\pi}{4}, \pi, \frac{5\pi}{4}, \frac{3\pi}{2}$ and $\frac{7\pi}{4}$. Since the ion lifetime is expected from previous studies to be only a few μs [6, 10, 42, 43], the period of the LF waveform (200 μs) is sufficiently long that the effects of varying the rf pulse position can be resolved. The closed circle in figure 6 and the waveforms shown previously in figure 4 correspond to a pulse position of $\frac{3\pi}{2}$, where the rf pulses are applied at the LF voltage minima. For all pulse positions, the LF and rf voltage amplitudes remain constant at 3.6 kV and 1.0 kV, respectively.

As shown in figure 6, the thrust is maximized when the rf pulses are positioned at the LF minima ($\frac{3\pi}{2}$: 3.1 mN m^{-1}) and this highlights the importance of negative ions in the generation of thrust as has been previously reported [12, 16, 19]. The thrust is also relatively large when the pulses are positioned at the LF maxima ($\frac{\pi}{2}$: 2.8 mN m^{-1}), but is weakest when the

pulses are positioned at its zero-crossings (phase positions of zero and π). The positions for which the largest thrust is observed therefore correspond to the times when the LF voltage V_{LF} is maximized.

Independent of the position of the rf pulses within the LF period, an increase in thrust between 0.3–1.5 mN m^{-1} is estimated when the rf-LF waveform drives the discharge compared to when no rf pulses are applied.

For constant rf voltage V_{rf} , when the rf pulse position is shifted within the period of the LF waveform, the peak voltage V_p can also change. For example, V_p is largest when the rf pulses are positioned at the LF maxima ($\frac{\pi}{2}$) or minima ($\frac{3\pi}{2}$), i.e. when $V_p = V_{LF} + V_{rf}$, and since $V_{rf} < V_{LF}$ (1.0 kV and 3.6 kV, respectively), equal to the LF voltage when the pulses are positioned at the LF zero-crossings. Since the mechanism for thrust in LF SDBDs is understood to be an exchange of momentum between ions and neutrals and the thrust increases for increasing values of V_{LF} , modulations in V_p could be expected to influence the thrust. However, due to the relatively high frequency of V_{rf} (MHz), the degree of ion drift within the rf pulses is relatively small compared to that which occurs as a result of V_{LF} (kHz). Hence the voltage component that is of primary importance to the ion drift is V_{LF} and its amplitude does not depend upon the rf pulse position. Similarly, the amplitude of V_{rf} is most influential to the production of ions and its amplitude is independent of the rf pulse position.

Therefore, for fixed amplitudes of V_{rf} and V_{LF} , modulations in V_p may not strongly influence either the production of ions by the rf field (in addition to those already generated by the LF field) nor the acceleration of ions by the LF field. They may therefore be of relatively minor importance to the variation in thrust that is observed when the position of the rf pulses is varied.

3.2. Spatially resolved flow properties

For the conditions in which the thrust generated by the rf-LF actuator is maximized, i.e. an LF waveform of amplitude 3.6 kV combined with 1.0 kV rf pulses positioned at the LF voltage minima (see closed circle in figure 6), velocity fields are acquired for increasing rf voltage and constant LF voltage. The velocity fields that are generated by the actuator are shown in figure 7 for rf pulses of (a) 0.0 kV, (b) 0.5 kV and (c) 1.0 kV.

As shown in figure 7(a), the actuator induces motion in the surrounding air with a maximum velocity $u_{x,max}$, measured in the direction tangential to the dielectric layer, of 0.46 m s^{-1} when no rf pulses are applied. The velocity u_x begins to increase for $x > 4 \text{ mm}$ from the edge of the powered electrode and this may be due to the presence of the discharge for $0 < x < 4 \text{ mm}$. As shown in figures 7(b) and (c), for increasing rf voltage $u_{x,max}$ increases to 0.53 m s^{-1} for 0.5 kV rf pulses and to 0.62 m s^{-1} for 1.0 kV rf pulses. The propagation of the actuation region in the x and y directions is also observed to increase for increasing rf voltage.

When the rf pulses are positioned at the maxima of the 3.6 kV LF waveform, similar increases in $u_{x,max}$ are observed with velocities of 0.51 m s^{-1} and 0.59 m s^{-1} measured for rf voltages of 0.5 kV and 1.0 kV, respectively.

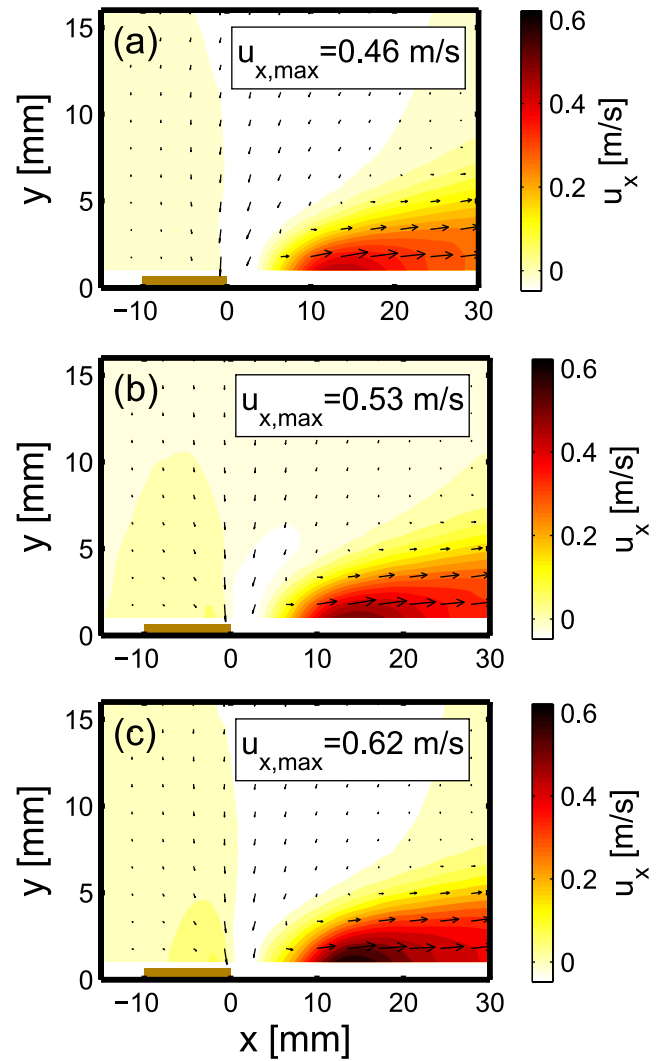


Figure 7. Velocity fields generated by the discharge when a 5 kHz, 3.6 kV LF voltage is combined with 5 kHz, $5 \mu\text{s}$ pulses of 13.56 MHz rf voltage of (a) 0.0 kV, (b) 0.5 kV and (c) 1.0 kV. The rf pulses are positioned at the LF voltage minima as marked by the closed circle in figure 6. The field-of-view for PIV is located approximately 1 mm above the surface of the dielectric layer, which is located at $y = 0 \text{ mm}$, and the location of the powered electrode is shown by the solid line (thickness not to scale). The direction of the total velocity (reduced spatial resolution for clarity) and magnitude of the velocity tangential to the dielectric layer u_x are shown by the arrows and colours, respectively.

3.3. Estimation of the discharge power

The power that is dissipated in the rf-LF discharge for the maximum-thrust condition, i.e. a 3.6 kV LF voltage with 1.0 kV rf pulses positioned at the LF minima as shown in figure 7(c), is estimated by determining the LF and rf powers separately and adding the results together. The average rf power that is coupled to the discharge is determined using a 30 dB directional coupler. This is installed between the rf generator and the matching network as shown in figure 1. Measurements of the forward and reflected voltages, together with a calibration of the rf generator and dB coupler into 50Ω (using a standing-wave-ratio meter) are used to estimate the average rf power by taking into consideration the pulse

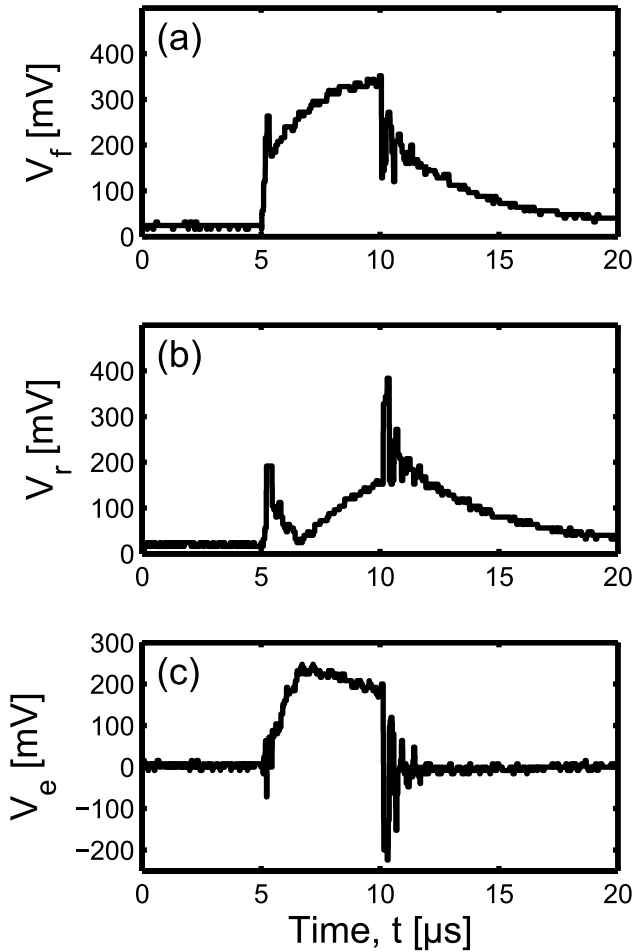


Figure 8. Envelopes of the (a) forward: V_f , (b) reflected: V_r and (c) effective: $V_e = V_f - V_r$ rf voltages as measured with the 30 dB directional coupler that is fitted between the rf generator and the matching network (see figure 1). Only the positive half of each envelope is shown to aid visualization.

duty cycle and envelope profile. The forward voltage V_f , as measured with the dB coupler during a representative rf pulse, is shown in figure 8(a). The reflected voltage V_r , shown in figure 8(b), is reduced to zero 1.5 μs into the pulse ($t = 6.5 \mu\text{s}$) and in a similar fashion to the rf current (see figure 3) exhibits spikes at the times when the generator is switching at $t = 5 \mu\text{s}$ and $t = 10 \mu\text{s}$.

The effective rf line voltage V_e , which is the difference between the forward and reflected voltages as shown in figure 8(c), is used with the power calibration to estimate the average effective rf power P_{rf} to be approximately 2.5 W. This is added to the average power dissipated in the LF discharge P_{LF} , which is estimated to be approximately 2 W using

$$P_{\text{LF}} \approx \frac{1}{T} \int_0^T V_d(t) I_{\text{rf}}(t) dt, \quad (3)$$

where T is the duration of one LF period (200 μs) and the discharge voltage V_d is approximated as the applied voltage (see figure 2 for the relevant waveforms) under the assumption that the voltage drop across the dielectric layer is small relative to that across the discharge [44]. The

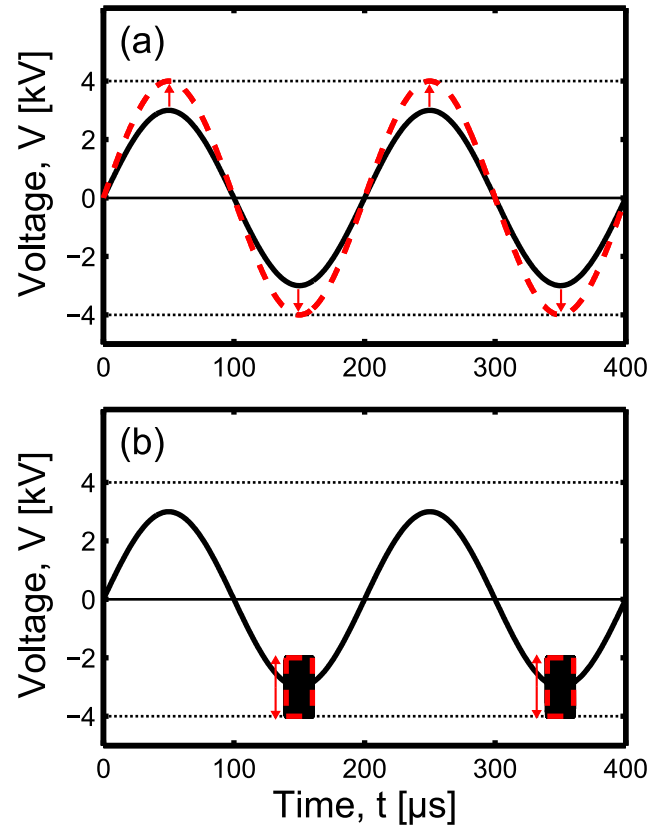


Figure 9. Illustration of the voltage waveforms at the powered electrode for (a) LF and (b) rf-LF discharges. The portions of the voltage waveform that are modified to achieve an increase in the peak voltage V_p (dotted lines) are shown by the dashed lines. For the rf-LF discharge, the rf pulses are applied at the LF voltage minima. The directions in which each waveform is modified are shown by the arrows.

total average power consumption is therefore estimated to be $P_{\text{tot}} \approx P_{\text{rf}} + P_{\text{LF}} \approx 4.5 \text{ W}$.

4. Efficacy compared to LF-driven actuators

As shown in figures 6 and 7, the thrust is observed to increase subsequent to the coupling of rf pulses to the LF-driven discharge. However, the electronics necessary to achieve this add complexity and weight to the actuator apparatus. It is therefore useful to determine whether the increase in thrust that is achieved through rf-LF actuation is larger or smaller than that which can be attained more simply by increasing the voltage of the LF waveform.

To investigate this point, the thrust that is generated using an LF driving voltage is estimated for increasing peak voltage V_p (for the LF-driven discharge $V_p = V_{\text{LF}}$). This is compared to that which is generated using an rf-LF waveform when the rf voltage is increased and LF voltage remains constant. These scenarios can both result in the same peak voltage as illustrated in figures 9(a) and (b), respectively.

The thrust T_x is plotted with respect to peak voltage V_p in figure 10 for the LF and rf-LF discharges. For the LF-driven discharge, the results of previous experimental studies suggest that the relationship between applied voltage and thrust follows the power law $T_x \sim V^{3.5}$ [24]. When the data for the LF

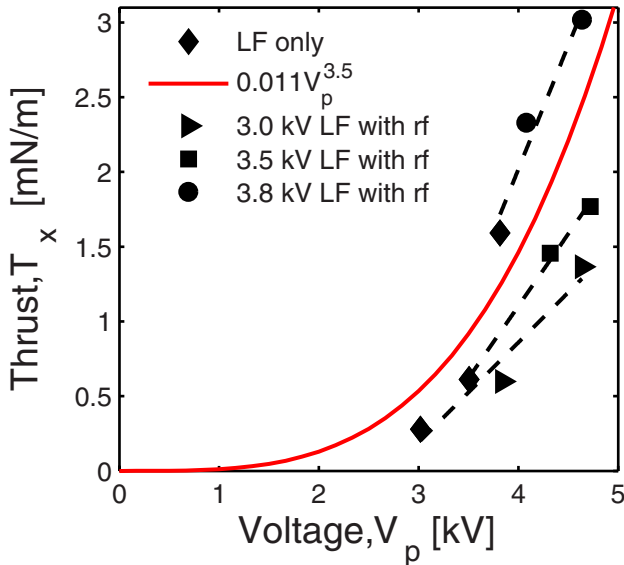


Figure 10. Variation in the thrust T_x with respect to peak voltage V_p for LF and rf-LF discharges. For the rf-LF discharge, rf pulses are applied at the LF voltage minima and V_p is increased by increasing the amplitude of the rf pulses while the amplitude of the LF waveform is fixed as shown in figure 9(b). The solid line shows a $T_x \sim V_p^{3.5}$ fit to the measurements for the LF discharge and the dashed lines are included to aid visualization.

discharge is fitted with a function of this form, the resultant curve can be thought of as a benchmark against which the rf-LF discharge is assessed. That is, for increased efficacy, the rf-LF discharge should generate a larger quantity of thrust per unit increase in V_p .

For the same values of V_{LF} that are applied to the LF-driven discharge, the thrust that is generated using the rf-LF driving waveform is shown in figure 10 for increasing rf voltage. The rf pulses are positioned at the LF voltage minima and so $V_p = V_{LF} + V_{rf}$. For constant V_{LF} , increases in V_p are achieved by increasing V_{rf} only as shown in figure 9(b).

As shown in figure 10, the application of rf pulses to the LF driving voltage results in an increased thrust for all values of V_p . However, for V_{LF} less than 3.8 kV, the thrust generated per unit increase in V_p using the rf-LF waveform is lower than that observed when the discharge is driven by an LF waveform only. For increasing values of V_{LF} , the efficacy of the rf-LF discharge increases and approaches that of the LF-driven discharge for $V_{LF} = 3.8$ kV. This can be explained by considering that when the electric field due to V_{LF} is relatively low, the degree to which any ions produced by the rf-driven discharge transfer their momentum to neutrals may also be low. As V_{LF} increases, the ions that are produced by the rf field are accelerated to a larger extent and this may result in a larger thrust. It can therefore be envisaged that for increasing V_{LF} , the thrust that is generated by the rf-LF discharge may increase further. Future work is therefore required to investigate this possibility at larger LF waveform voltages.

5. Conclusion

The effect of combining pulses of radio-frequency (rf: 13.56 MHz) voltage with a low-frequency (LF: 5 kHz) voltage

waveform in a surface dielectric barrier discharge actuator is investigated with respect to the generation of thrust. The thrust is found to be dependent upon the amplitude of the rf and LF voltages and the position of the rf pulses within the period of the LF voltage waveform. Maximum thrust in the direction tangential to the dielectric layer is achieved when the rf pulses are positioned at the LF voltage minima. The application of an rf-LF driving voltage is demonstrated to increase the thrust that is generated by the actuator, and the thrust that is generated per unit increase in peak voltage is observed to increase for increasing LF voltage.

Acknowledgments

The authors wish to thank P Alexander, S Holgate and D Tempra for their technical assistance and D Hong and H Rabat for many useful discussions. J Dedrick would also like to thank the SP3 Laboratory and The Australian National University (BT Scholarship) for their financial support.

References

- [1] Moreau E 2007 Airflow control by non-thermal plasma actuators *J. Phys. D: Appl. Phys.* **40** 605–36
- [2] Corke T C, Lon Enloe C and Wilkinson S P 2010 Dielectric barrier discharge plasma actuators for flow control *Ann. Rev. Fluid Mech.* **42** 505–29
- [3] Little J, Nishihara M, Adamovich I and Samimy M 2010 High-lift airfoil trailing edge separation control using a single dielectric barrier discharge plasma actuator *Exp. Fluids* **48** 521–37
- [4] Jukes T N and Choi K S 2012 Dielectric-barrier-discharge vortex generators: characterisation and optimisation for flow separation control *Exp. Fluids* **52** 329–45
- [5] Benard N and Moreau E 2013 Response of a circular cylinder wake to a symmetric actuation by non-thermal plasma discharges *Exp. Fluids* **54** 1467
- [6] Macheret S O, Shneider M N and Miles R B 2002 Modeling of air plasma generation by repetitive high-voltage nanosecond pulses *IEEE Trans. Plasma Sci.* **30** 1301–14
- [7] Opaitis D F, Likhanskii A V, Neretti G, Zaidi S, Shneider M N, Miles R B and Macheret S O 2008 Experimental investigation of dielectric barrier discharge plasma actuators driven by repetitive high-voltage nanosecond pulses with dc or low frequency sinusoidal bias *J. Appl. Phys.* **104** 043304
- [8] Starikovskii A Y, Nikipelov A A, Nudnova M M and Roupasov D V 2009 SDBD plasma actuator with nanosecond pulse-periodic discharge *Plasma Sources Sci. Technol.* **18** 034015
- [9] Unfer T and Boeuf J P 2009 Modelling of a nanosecond surface discharge actuator *J. Phys. D: Appl. Phys.* **42** 194017
- [10] Boeuf J P and Pitchford L C 2005 Electrohydrodynamic force and aerodynamic flow acceleration in surface dielectric barrier discharge *J. Appl. Phys.* **97** 103307
- [11] Boeuf J P, Lagmich Y, Unfer Th, Callegari Th and Pitchford L C 2007 Electrohydrodynamic force in dielectric barrier discharge plasma actuators *J. Phys. D: Appl. Phys.* **40** 652–62
- [12] Boeuf J P, Lagmich Y and Pitchford L C 2009 Contribution of positive and negative ions to the electrohydrodynamic force in a dielectric barrier discharge plasma actuator operating in air *J. Appl. Phys.* **106** 023115

- [13] Im S, Do H and Cappelli M A 2012 The manipulation of an unstarting supersonic flow by plasma actuator *J. Phys. D: Appl. Phys.* **45** 485202
- [14] Roy S 2005 Flow actuation using radio frequency in partially ionized collisional plasmas *Appl. Phys. Lett.* **88** 101502
- [15] Lagmich Y, Callegari Th, Unfer Th, Pitchford L C and Boeuf J P 2007 Electrohydrodynamic force and scaling laws in surface dielectric barrier discharges *Appl. Phys. Lett.* **90** 051502
- [16] Kim W, Do H, Mungal M G and Cappelli M A 2007 On the role of oxygen in dielectric barrier discharge actuation of aerodynamic flows *Appl. Phys. Lett.* **91** 181501
- [17] Singh K P and Roy S 2007 Modeling plasma actuators with air chemistry for effective flow control *J. Appl. Phys.* **101** 123308
- [18] Singh K P and Roy S 2008 Physics of plasma actuator operating in atmospheric air *Appl. Phys. Lett.* **92** 111502
- [19] Kotsonis M and Ghaemi S 2011 Forcing mechanisms of dielectric barrier discharge plasma actuators at carrier frequency of 625 Hz *J. Appl. Phys.* **110** 113301
- [20] Debien A, Benard N, David L and Moreau E 2012 Unsteady aspect of the electrohydrodynamic force produced by surface dielectric barrier discharge actuators *Appl. Phys. Lett.* **100** 013901
- [21] Neumann M, Friedrich C, Czarske J, Kriegseis J and Grundmann S 2013 Determination of the phase-resolved body force produced by a dielectric barrier discharge plasma actuator *J. Phys. D: Appl. Phys.* **46** 042001
- [22] Hoskinson A R and Hershkowitz N 2010 Differences between dielectric barrier discharge plasma actuators with cylindrical and rectangular exposed electrodes *J. Phys. D: Appl. Phys.* **43** 065205
- [23] Debien A, Benard N and Moreau E 2012 Streamer inhibition for improving force and electric wind produced by DBD actuators *J. Phys. D: Appl. Phys.* **45** 215201
- [24] Thomas F O, Corke T C, Iqbal M, Kozlov A and Schatzman D 2009 Optimization of dielectric barrier discharge plasma actuators for active aerodynamic flow control *AIAA J.* **47** 2169–78
- [25] Durscher R and Roy S 2012 Aerogel and ferroelectric dielectric materials for plasma actuators *J. Phys. D: Appl. Phys.* **45** 012001
- [26] Forte M, Jolibois J, Pons J, Moreau E, Touchard G and Cazalens M 2007 Optimization of a dielectric barrier discharge actuator by stationary and non-stationary measurements of the induced flow velocity: application to airflow control *Exp. Fluids* **43** 917–28
- [27] Balcon N, Benard N, Lagmich Y, Boeuf J-P, Touchard G and Moreau E 2009 Positive and negative sawtooth signals applied to a DBD plasma actuator—influence on the electric wind *J. Electrostat.* **67** 140–5
- [28] Benard N and Moreau E 2010 Capabilities of the dielectric barrier discharge plasma actuator for multi-frequency excitations *J. Phys. D: Appl. Phys.* **43** 145201
- [29] Benard N and Moreau E 2012 Role of the electric waveform supplying a dielectric barrier discharge plasma actuator *Appl. Phys. Lett.* **100** 193503
- [30] Kotsonis M and Ghaemi S 2012 Performance improvement of plasma actuators using asymmetric high voltage waveforms *J. Phys. D: Appl. Phys.* **45** 045204
- [31] Moreau E, Sosa R and Artana G 2008 Electric wind produced by surface plasma actuators: a new dielectric barrier discharge based on a three-electrode geometry *J. Phys. D: Appl. Phys.* **41** 115204
- [32] Benard N, Mizuno A and Moreau E 2009 A large-scale multiple dielectric barrier discharge actuator based on an innovative three-electrode design *J. Phys. D: Appl. Phys.* **42** 235204
- [33] Berendt A, Podliński J and Mizeraczyk J 2011 Elongated DBD with floating interelectrodes for actuators *Eur. Phys. J. Appl. Phys.* **55** 13804
- [34] Park J, Henins I, Herrmann H W and Selwyn G S 2001 Gas breakdown in an atmospheric pressure radio-frequency capacitive plasma source *J. Appl. Phys.* **89** 15–9
- [35] Kim D B, Rhee J K, Gweon B, Moon S Y and Choe W 2007 Comparative study of atmospheric pressure low and radio frequency microjet plasmas produced in a single electrode configuration *Appl. Phys. Lett.* **91** 151502
- [36] Allegraud K, Guaitella O and Rousseau A 2007 Spatio-temporal breakdown in surface DBDs: evidence of collective effect *J. Phys. D: Appl. Phys.* **40** 7698–706
- [37] Pons J, Moreau E and Touchard G 2005 Asymmetric surface dielectric barrier discharge in air at atmospheric pressure: electrical properties and induced airflow characteristics *J. Phys. D: Appl. Phys.* **38** 3635–42
- [38] Durscher R and Roy S 2012 Evaluation of thrust measurement techniques for dielectric barrier discharge actuators *Exp. Fluids* **53** 1165–76
- [39] Kotsonis M, Ghaemi S, Veldhuis L and Scarano F 2011 Measurement of the body force field of plasma actuators *J. Phys. D: Appl. Phys.* **44** 045204
- [40] Kriegseis J, Schwarz C, Tropea C and Grundmann S 2013 Velocity-information-based force-term estimation of dielectric-barrier discharge plasma actuators *J. Phys. D: Appl. Phys.* **46** 055202
- [41] Hoskinson A R, Hershkowitz N and Ashpis D E 2008 Force measurements of single and double barrier DBD plasma actuators in quiescent air *J. Phys. D: Appl. Phys.* **41** 245209
- [42] Kossyi I A, Kostinsky A Yu, Matveyev A A and Silakov V P 1992 Kinetic scheme of the non-equilibrium discharge in nitrogen–oxygen mixtures *Plasma Sources Sci. Technol.* **1** 207–20
- [43] McGowan S 1965 Ion–ion recombination in laboratory air *Phys. Med. Biol.* **10** 25–40
- [44] Dong B, Bauchire J M, Pouvesle J M, Magnier P and Hong D 2008 Experimental study of a DBD surface discharge for the active control of subsonic airflow *J. Phys. D: Appl. Phys.* **41** 155201